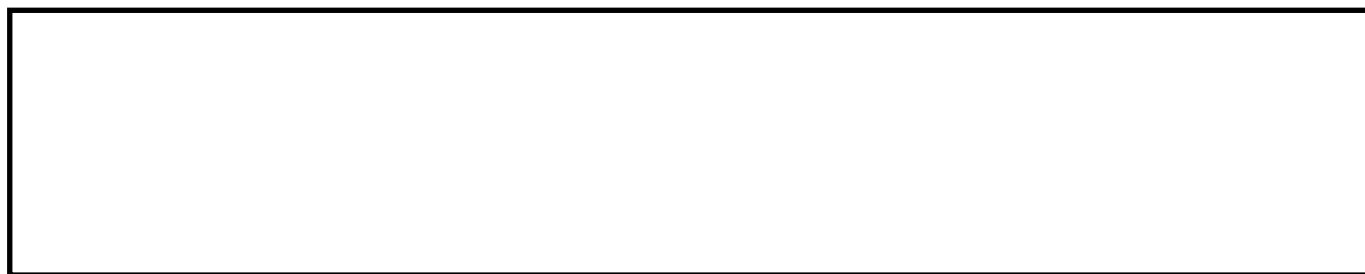


WANG, S., TAKYI-ANINAKWA, P., JIN, S., YU, C., FERNANDEZ, C. and STROE, D.-I. 2022. An improved feedforward-long short-term memory modeling method for the whole-life-cycle state of charge prediction of lithium-ion batteries considering current-voltage-temperature variation. *Energy* [online], 254(Part A), article 124224. Available from: <https://doi.org/10.1016/j.energy.2022.124224>

An improved feedforward-long short-term memory modeling method for the whole-life-cycle state of charge prediction of lithium-ion batteries considering current-voltage-temperature variation.

WANG, S., TAKYI-ANINAKWA, P., JIN, S., YU, C., FERNANDEZ, C. and STROE, D.-I.

2022



An improved feedforward-long short-term memory modeling method for the whole-life-cycle state of charge prediction of lithium-ion batteries considering current-voltage-temperature variation

Shunli Wang¹, Paul Takyi-Aninakwa¹, Siyu Jin², Chunmei Yu¹, Carlos Fernandez³, Daniel-Ioan Stroe²

¹*School of Information Engineering & Robot Technology Used for Special Environment Key Laboratory of Sichuan Province, Southwest*

University of Science and Technology, Mianyang 621010, China. ²*Department of Energy Technology, Aalborg University, Pontoppidanstraede*

111 9220 Aalborg East, Denmark. ³*School of Pharmacy and Life Sciences, Robert Gordon University, Aberdeen AB10-7GJ, UK.*

Abstract: The whole-life-cycle state of charge (SOC) prediction plays a significant role in various applications of lithium-ion batteries, but with great difficulties due to their internal capacity, working temperature, and current-rate variations. In this paper, an improved feedforward-long short-term memory (FF-LSTM) modeling method is proposed to realize an accurate whole-life-cycle SOC prediction by effectively considering the current, voltage, and temperature variations. An optimized sliding balance window is constructed for the measured current filtering to establish a new three-dimensional vector as the input matrix for the filtered current and voltage. Then, an improved steady-state screening model is constructed for the predicted SOC redundancy reduction that is obtained by the Ampere-hour integral method and taken as a one-dimensional output vector. The long-term charging capacity decay tests are conducted on two batteries, C7 and C8. The results show that the battery charging capacity reduces significantly with increasing time, and the capacity decreases by 21.30% and 22.61%, respectively, after 200 cycles. The maximum whole-life-cycle SOC prediction error is 3.53% with RMSE, MAE, and MAPE values of 3.451%, 2.541%, and 0.074%, respectively, under the complex DST working condition. The improved FF-LSTM modeling method provides an effective reference for the whole-life-cycle SOC prediction in battery system applications.

Keywords: whole-life-cycle state of charge; lithium-ion battery; capacity fading; feedforward-long short-term memory; sliding balance window; steady-state screening model

***Corresponding author:** Shunli Wang, wangshunli@swust.edu.cn.

Highlights:

- Improved feedforward-long short-term memory (FF-LSTM) modeling for SOC prediction
- Sliding balance window of dimensional current-voltage-temperature variation vectors
- Optimized steady-state screening model built with Ah integration and output vector
- Whole-life-cycle feature analysis for current, voltage, temperature, and capacity

1. Introduction

With the development of new energy technologies, lithium-ion batteries have been widely used in complex power supply conditions. How to predict the battery's state accurately under complex working conditions has also become a global challenge that needs to be solved urgently. The inevitable aging process of lithium-ion batteries negatively affects the safe and stable operation of energy storage systems [1-3]. An accurate state of charge (SOC) prediction is required to realize the remaining energy prediction, real-time power management, and service life extension. The chemical causes of the aging process are analyzed for lithium-ion batteries by considering the influence of environmental temperature variations with a feedforward migration neural network to achieve a long battery life [4]. The aging data set is also used to train the feedforward neural network for the aging trajectory prediction.

Lithium-ion batteries have strong nonlinear dynamic characteristics due to the internal coupling reaction process. The degradation mechanisms are investigated by differential voltage analysis with the alternating current impedance [5]. Also, the working environment, series-parallel circuit network, and application conditions affect the operation of the batteries significantly [6-9]. Considering the battery aging process, predictive energy management is necessary for the aging and temperature characterization with active and adaptive aging prediction, so an adaptive equivalent consumption minimization strategy is constructed with a recurrent neural network (AECMS-RNN) [10]. The characteristic features are extracted based on the parameter and state variations during the reaction. The mathematical expression is formed to simulate the steady-state and dynamic response characteristics of the batteries [11]. A new quantitative aging model is established by performing the state-space

expression, and the battery aging changes are realized by the fractional difference expression [12]. Based on this modeling strategy, the aging characteristics of lithium-ion batteries are extracted for the sub-zero temperature conditions to establish a robust capacity decay prediction model [13-15]. Also, the method of constructing the working process function has good applicability based on the correlation between the charge-discharge current rates and the closed-circuit voltage (CCV) variation [16]. This method is suitable for processing characterization, thermal conductivity description, temperature simulation, and aging effect expression [17-19]. Combining the sensitivity and thermal mechanism analysis [20], the effective characterization of battery performance degradation under wide temperature variations has become the mainstream of modeling for the series-parallel optimizing method, which is an essential solution for accurate battery state characterization.

Most of the modeling methods are concerned with single influencing factors, and the research on the multi-parameter coupling mechanism has not matured under the influence of multiple factors. The performance parameters of different charge-discharge stages vary significantly, and the influencing factors between battery cells change obviously [21]. Therefore, considering the multi-factor coupling and the periodic changing law, it is an effective way to balance the modeling accuracy and complexity. It is also used to explore the influence of the parameter changes and mutual variation degree while obtaining the parameter description law and optimization method in different modes [22]. Multiple cells are connected in series to improve the voltage level, in which case there are negative effects such as short-circuiting [23]. These serious problems are caused by the cell-to-cell difference that needs to be characterized accurately, so the capacity fading process is an essential characteristic for the mathematical description of the lithium-ion battery model to optimize the energy supply capabilities [24]. The capacity fading mechanism analysis is carried out [25], and its attenuation monitoring is conducted using optical fibers [26]. The current density of the defect-induced capacity attenuation is introduced through the local electroplating of lithium-ion batteries [27]. Capacity decay and cyclic aging are considered at various SOC levels [28], in which the changes in lithium-ion concentration are taken into consideration to get the capacity decay

mechanism.

The open-circuit voltage (OCV) highly affects the terminal voltage of lithium-ion batteries, and the working state change is used as the main influencing factor for their working condition monitoring. Through the OCV characteristic relationship analysis, the aging diagnosis is realized online for lithium-ion batteries [29]. Also, the aging mechanism is highly influenced by the OCV characteristic analysis of the half-cell and full-cell levels, which is considered to conclude the aging mechanisms towards cell capacity reduction. [30]. The fast-charging effect is analyzed for lithium-ion batteries when working at low-temperature conditions, in which the fast charging effects are investigated on the performance of a high-energy cell [31]. The state of power (SOP) is predicted under the maximum operating temperature constraint by introducing various temperature indication methods into the state prediction process by analyzing the temperature dependence of the lithium electroplating phenomenon [32]. The cyclic stability is analyzed for lithium-ion batteries under high working temperature levels [33], which shows that the capacity decays fast at 60 °C and the capacity retention rate is as low as 47% after 100 cycles.

In the battery modeling process, it is necessary to determine the core parameters and introduce them into the real-time state monitoring process. The co-prediction of model parameters and SOC is performed with recursive restricted total least squares (RRTLS) [34] and the unscented Kalman filtering (UKF) method [35]. Also, an improved adaptive dual unscented Kalman filter (DUKF) is proposed for online parameter identification and SOC prediction [36]. The online parameter identification is carried out through the improved instrument variable prediction [37] and the impedance-based diagnosis [38, 39], including the multiple output correlation and vector regression to identify the physical parameters. Based on the simplified electrochemical modeling and aging mode analysis, the physical parameter identification is carried out effectively [40]. The parameter identification is established with an improved recursive least square (RLS) method by multiple-time inner loop update of the parameter vector [41]. The online complexity reduction parameter prediction technology is introduced into the equivalent circuit modeling process [42], and the aging model is built [43] by introducing the multidisciplinary

parameters.

The state prediction of lithium-ion batteries can be realized by the characteristic analysis, which is useful for the effective energy supply process throughout the whole life-cycle aging process. On the discharge curves, both the state of health (SOH) and remaining useful life (RUL) are estimated accurately in real-time by combining the electrochemistry-based electrical and semi-empirical capacity fading models [44]. Based on the extended state observer of a generalized proportional-integral type, a reliable SOC prediction is observed for lithium-ion batteries [45]. The battery modeling is established by considering the hysteresis effect based on an improved Coulomb counting method [46]. Combined with the support vector machine (SVM) [47], the Gaussian process (GP)-Bayesian filters [48] are constructed for the SOC monitoring of lithium-ion batteries. For an effective energy supply process, the battery management methods are analyzed under complex working conditions. A numerical simulation of a multi-micro channel radiator is introduced to research thermal management system. The effect of phase change and heat pipe coupling is carried out on the performance enhancement in the thermal management system. Thermal safety management includes current issues and opinions by the application of tree-like micro-channel heat sinks and numerical optimization [49]. The reduction of the qualifying time is characterized through state prediction and health management, in which the anomalies in the capacity fade curve of unhealthy batteries can be detected by analyzing the fading trend [50]. The thermal management performance is studied to provide an effective way to manage the temperature in the battery packs [51].

The overall modeling method ignores the internal electrochemical reactions and the cell-to-cell difference, making it suitable for battery modeling in complex conditions. A battery model is established under different working conditions by considering the influence of temperature on capacity and internal resistance [52]. The cut-off voltage adopts the cell's first cut-off voltage during the charge-discharge process with simplicity and easy implementation advantages. The self-discharge rate difference is also considered with the internal resistance and capacity variations. The average difference modeling method obtains the electrical parameters based on the

average arithmetic method, which superimposes the difference to correct the key parameter variation, such as the impact of high-power charging on safety [53], to realize the dynamic characterization. It also accurately describes the differences between battery cells with the coupling relationship between current magnification and capacity [54]. The influencing mechanisms are discussed for internal resistance, SOC, and the external environment on the current distribution. The battery data is compressed and reconstructed using the frequency division multiplexing principle [55-58], according to which the prediction methods are analyzed with numerical simulation for effective correction of the model parameters.

The electrochemical analysis of battery aging and capacity decay effects are investigated, and life cycle comparison and evaluation are conducted to solve the capacity decay problem in EVs. The influence of the increase in resistance due to capacity decay is analyzed to establish a global self-discharge model for lithium-ion batteries [60]. By considering the capacity attenuation, the capacity decay of the long battery life is analyzed for the buffer application of EV superchargers [61]. The electric bus fleet is dispatched optimally by the dynamic mathematical programming, as it experiences capacity decays and thermal stability after overcharging [59]. A comprehensive model has been developed to describe the Coulomb efficiency and capacity decays under different aging conditions.

By considering the current, voltage, and temperature variations, an improved feedforward-long short-term memory (FF-LSTM) modeling method is proposed to guarantee the whole-life-cycle SOC prediction performance. An improved sliding balance window is established for the measured current filtering so that a new three-dimensional vector is constructed for the filtered current and voltage. An optimized steady-state screening model is constructed for the predicted SOC value based on the Ampere-hour integral method as a one-dimensional output vector. The long-term dynamic stress test procedure is designed for the training process. A special three-dimensional current, voltage, and temperature variation procedure is designed for the variable temperature capacity test, composite OCV measurement, hybrid pulse power characterization (HPPC) test, and the dynamic

stress test for experimental verification.

2. Mathematical analysis

The improved FF-LSTM modeling method is proposed by considering the current, voltage, and temperature variations. An improved sliding balance window is established for the measured current value filtering, with an improved steady-state screening model is constructed as a one-dimensional output vector. A pulse-current test procedure is designed, including the capacity, OCV, and other parameters in the whole-life-cycle working condition simulation to express the fading process.

2.1. Improved feedforward-long short-term memory method

Based on the frame network structure, the functional expression is designed for different output levels and internal parameter coupling relationship characterization. The aging characteristics are considered in the iterative calculation procedure for the current, SOC, and temperature, which are used to establish a processing model that reflects the working characteristics and the present weighting coefficient. The variation law of the ohmic resistance and polarization effects are explored with the phased expression of the instantaneous voltage rise, deceleration, and stabilization after the current interruption. The FF-LSTM training and correction sub-model is constructed to realize the step-by-step prediction, as shown in Figure 1.

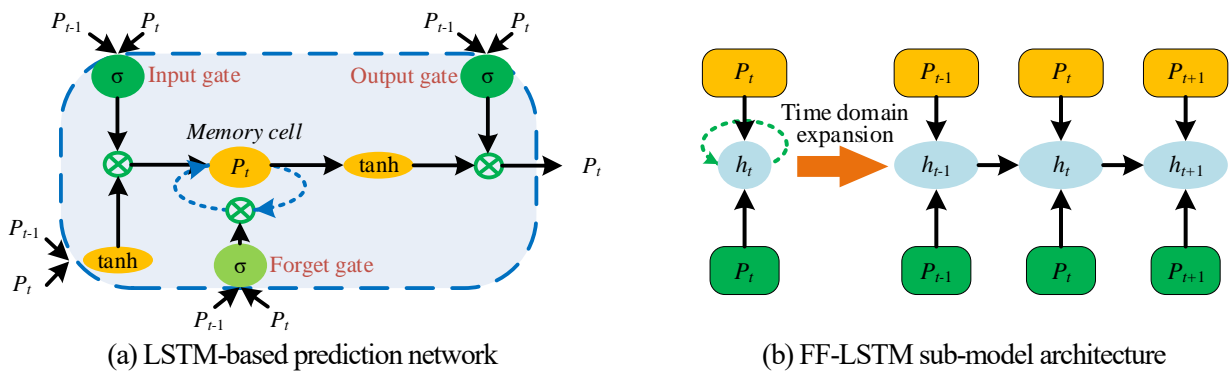


Figure 1. The FF-LSTM-based long-term SOC prediction and correction

In Figure 1, the equivalent parameters are introduced into the iterative calculation procedure by constructing the state-space equations to realize the accurate working characteristic description. Based on the capacity

attenuation process, multi-stress failure processing is conducted. The improved sliding balance window is used to update the model parameters in real-time and characterize the degradation trend effectively. Two state factors are introduced into the FF-LSTM model, including the information from the cell state C_t and the hidden state h_t . The present cell state is formed by considering the cell state C_{t-1} at time point $t - 1$ and the extracted information from the input parameters. The forget gate f_t is used to determine which state information should be discarded. Then, the information continues to the cell state with the present input signals of the prediction procedure design, as shown in Equation (1).

$$f_t = \sigma(W_f[h_{t-1}, x_t]) + b_f \quad (1)$$

In Equation (1), t is the information update time point, and f_t is the output of the forget gate, which determines whether information from the input data x_t and hidden state h_{t-1} should be retained or discarded. W_f is the weighting coefficient; h_{t-1} is the hidden state output of the cell at time point $t - 1$; x_t is the input parameter at the time point t ; b_f is the bias vector; $\sigma(*)$ is a sigmoid function that is used to make the output value vary from 0 to 1, where 1 means retaining and 0 means discarding the information.

The next step is to determine which information should be retained and introduced into the network at time point t using the input gate, which is divided into the following two parts. Firstly, a sigmoid layer is designed for the input gate, which determines the updated information and the discarded information. Secondly, the \tanh layer creates a cell state vector \tilde{C}_t for the new information, which is used to update the cell state information by multiplying these two parts, as shown in Equation (2).

$$\begin{cases} i_t = \sigma(W_i[h_{t-1}, x_t]) + b_i \\ \tilde{C}_t = \tanh(W_c[h_{t-1}, x_t]) + b_c \end{cases} \quad (2)$$

In Equation (2), W_i and W_c are two weighting coefficients for the input gate, and b_i and b_c are two bias vectors for the input gate and memory cell, respectively. Then, the combination vector of these two states is introduced into the \tanh layer, according to which the candidate input state of the present cell state \tilde{C}_t is established. Finally,

the cell state C_{t-1} at the previous time point and the present input cell state \tilde{C}_t are multiplied by the forget gate and the input gate to obtain the present cell state C_t , as shown in Equation (3).

$$C_t = f_t * C_{t-1} + i_t * \tilde{C}_t \quad (3)$$

In Equation (3), combining the past cell state C_{t-1} and the forget gate f_t with the point-wise multiplication of the input gate and the cell state vector \tilde{C}_t , the present cell state C_t is established. The output gate determines the information released from the cell state, which is also the memory cell information state passed on to the next cell of the network. The candidate cell state is introduced into the \tanh layer combined with the output gate, which is then multiplied by the output information of the sigmoid function to establish the output gate, as shown in Equation (4).

$$\begin{cases} o_t = \sigma(W_0[h_{t-1}, x_t]) + b_0 \\ h_t = O_t * \tanh(C_t) \end{cases} \quad (4)$$

In Equation (4), o_t is the information of the output gate at time point t and W_0 is the weighting coefficient of the output gate. b_0 is the bias vector of the output gate, $\sigma(*)$ is a sigmoid function, and h_t is the final output information. Consequently, the adaptability of the dynamic timing part of the observation input is improved, and the long-term dependence problem is eliminated. Compared with the original modeling method, the improved method introduces the dependence feature of the time series data into the inner network so that the dependency relationship is fully considered in the prediction process. By introducing the cell state C_t , both the outside cycle between the networks in the hidden layer and the self-circulation in the inner cell state are effectively realized.

The cell state is the crux that penetrates both the input layer and the output layer, in which the information flow changes slightly. Consequently, the cell state is updated using these three gates so that the information is stored accurately. The discrete dynamic modeling structure is established and optimized by considering the current fluctuation and ambient temperature influence. Prediction accuracy is ensured with limited data provided by the battery system in the early stages. Therefore, it is relatively difficult to explore the implicit relationship deeply

between aging inducement, multi-parameter prediction, and SOC levels. Over time, the data scale and quality available for the network's training is gradually improved, which synchronously improves the SOC prediction accuracy. The training and testing of the FF-LSTM method are conducted using a stochastic gradient optimizer, the adaptive moment estimate (Adam), which is computationally efficient and has little tuning and low memory requirements. The gradient (β_1) and squared gradient (β_2) decay rates are defined as 0.9 and 0.999, respectively. A learning rate of 0.01 and a batch size of 64 are set based on the performance of the network during the training and testing. Also, a gradient threshold of 1 and a decay rate of 0.95 are used to train the network for SOC prediction.

2.2. Real-time sliding balance window functional adaptation

Combined with the correction of key parameters and weighting factors, the intermittent aging degree evaluation and real-time correction are conducted. The sliding balance window function is introduced to obtain the prediction results and improve the model construction continuously to realize the prediction-correction process, as shown in Figure 2.

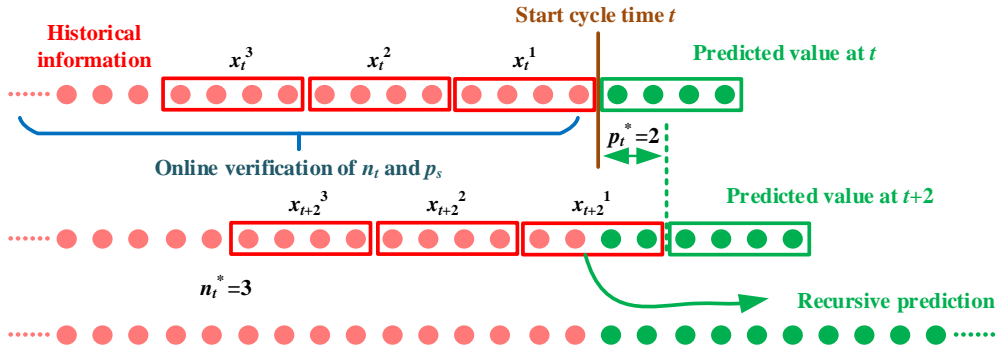


Figure 2. Prediction-correction process based on sliding balance window function

In Figure 2, considering the influence of sliding window size on calculation complexity and accuracy, through comparative analysis of test results, its value is set to 4 to achieve good results with less computational cost. The measurement experiment of the standard charge-discharge capacity is carried out with the Ampere-hour integral method to obtain the discharged capacity Q_n . SOC_n is used to describe the SOC value mathematically during the charge-discharge process. The rated capacity Q_{n_R} is characterized by SOC_0 , and the relative change ratio is

calculated by taking δ_S as the influencing coefficient, as shown in Equation (5).

$$\begin{cases} K_Q = \delta_S = \frac{SOC_n}{SOC_0} \times 100\% = \frac{Q_{n_D}}{Q_{0_R}} \times 100\% \\ Q_n = K_Q Q_{n_R} - \Delta Q_n, \Delta Q_n = f(N) \end{cases} \quad (5)$$

In Equation (5), n is the cycle number for the latest capacity measurement; ΔQ_n is the subsequent charge-discharge influence on the rated capacity. The initial value of the full charge is obtained by the balance-charging treatment, and Q_n is designed by considering the slow change characteristics of the aging process. The influencing coefficient K_Q is introduced to realize the normalized characterization of Q_n . Through the synchronous correlation between the rated capacity and cycling number, the functional relationship is obtained to calculate ΔQ_n . By considering the aging factor's influence on the rated capacity, these two parts are superimposed to obtain the corrected value of Q_n . For the measurement target of Q_n , the initial value SOC_0 after the full charge in the constant current-constant voltage (CC-CV) mode is used to replace Q_{n_R} .

2.3. Feedback correction framework

Considering the relationship between the model parameters, current rate, and temperature, the feedback correction framework of the prediction process is constructed. Based on the correction of the temperature and current magnification, the modeling performance evaluation is conducted to improve the model with the accuracy and adaptability of the SOC prediction. The data preprocessing, feature vector extraction, selection of training set, and validation set are expressed, as shown in Figure 3.

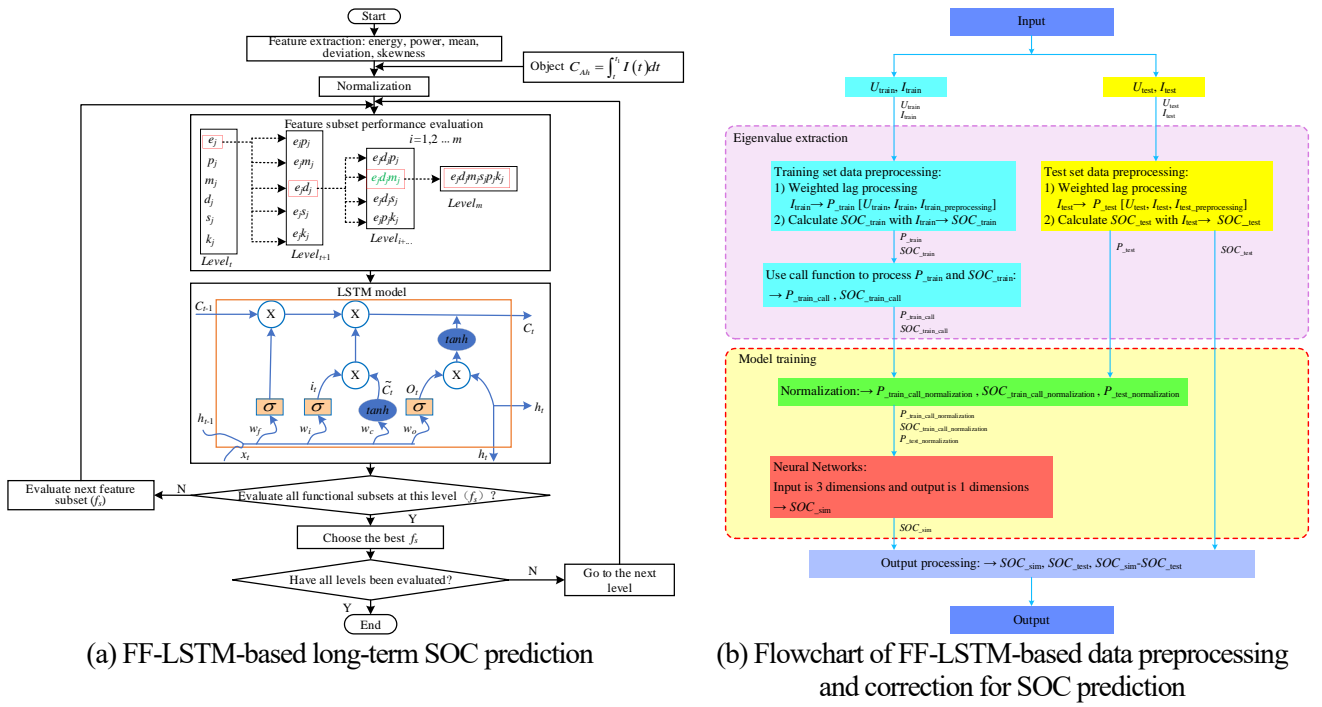


Figure 3. FF-LSTM-based long-term SOC prediction and data preprocessing correction

In Figure 3, the model parameters, state variables, and variance are updated in the cyclic iteration process in real-time to improve the SOC prediction robustness and enhance the modeling adaptability for complex working conditions. For the uncertainty noise, the internal resistance is estimated with a controlled error range to improve the stability and convergence of the FF-LSTM-based prediction network. The data preprocessing and SOC are carried out synchronously to ensure the accuracy of the constructed FF-LSTM network, which improves the prediction accuracy and reduces the computational complexity in the training process.

2.4. Composite OCV-HPPC evaluation procedure

The approximate current rate and temperature change tests are conducted, in which the main parameters are obtained through dynamic stress tests closely related to real-time working conditions. The fading process is described effectively by considering the effects of varying temperatures and current rates. So the improved test procedure is performed using the flexible feature with the real-time state monitoring of lithium-ion batteries. During the capacity test, the battery is filled with power at a current rate of 1 C using the CC-CV charging mode. Then, it is discharged to the cut-off voltage at a current rate of 0.3 C. This step is repeated three times throughout the succession at varying temperatures and current rates. The procedure of the capacity and the HPPC tests are

performed, as shown in Figure 4.

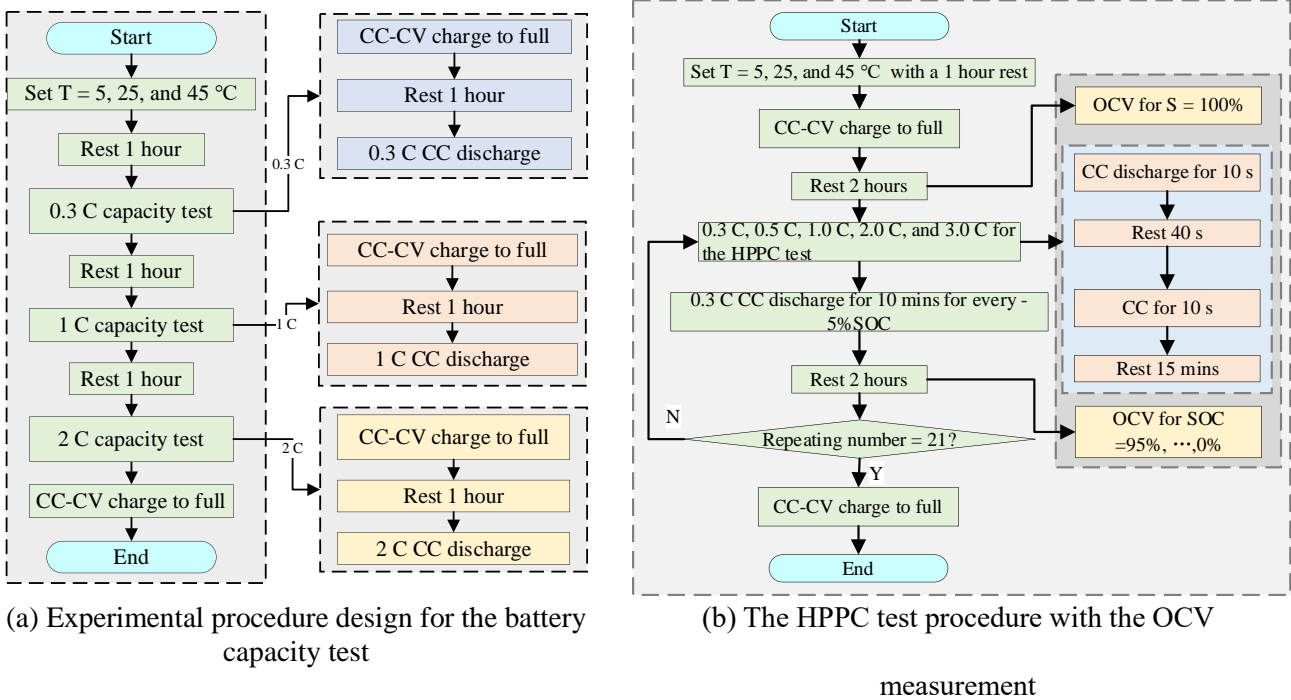


Figure 4. The experimental procedure for the battery capacity test and the HPPC test with the OCV

measurement

In Figure 4, the battery is rested for 1 hour after the chamber is set to be stable in the exposed temperature conditions. The aim is to make the initial temperature of the battery the same as the chamber temperature. Then, the 0.3 C capacity test is conducted to get the accurate capacity to fully charge the battery and discharge it at a current rate of 0.3 C after the 1-hour rest period. Then, the 1 C capacity test is conducted after the 1-hour rest, in which a 1 C current rate is used for the charge-discharge pulse. The 2 C capacity test is conducted on the battery with the 2 C fast discharge current rate using the CC pulse mode. Finally, the battery is fully charged using the CC-CV charging mode, which always leaves the battery in a good state.

Combining these two parts is computationally efficient since the battery should be rested for a long time in both the HPPC test and OCV measurement. Consequently, the pulse rest period is used in both the OCV measurement and the HPPC test to obtain the dynamic characteristics for the continuous pulse excitation sequence.

The combined test procedure is designed for the HPPC test and OCV measurement. The composite testing procedure is designed for different temperature conditions, in which the HPPC, OCV measurement, and variable temperature parameters are introduced into the training process. The temperature condition is set by the chamber setting, including 2, 25, and 45 °C. Then, the battery is rested for 1 hour to realize the thermal exchange and inside-outside balance. The battery is charged to full capacity using the CC-CV pulse. The rest time is set to be 2 hours for an accurate OCV determination, the value of which can be measured after this long-time process. Then, the HPPC test and OCV measurement are conducted every 21 cycles, as the battery energy is discharged for 5% recycling time in the whole pulse-current discharging process.

Multiple current rates of the HPPC test are conducted, including 0.3, 0.5, 1.0, 2.0, and 3.0 C, to obtain experimental data. In the HPPC test, the pulse-current charge-discharge treatments are conducted, including the CC discharge for 10 s, rested for 40 s, CC charge for 10 s, and rested for 15 min. The last long-time rest is to ensure the electrochemical and thermal equilibrium of the state of the battery before the next HPPC test profile. After the multiple current-rate tests, the battery is rested again for 2 hours so that the intermittent OCV and HPPC tests are completed, and the battery characteristics are obtained for different SOC levels, such as 95%, 90%, 85%, ..., 0%. After 21 cycling tests, the battery is fully charged before the next test using the CC-CV charging pulse, providing an effective approach to the battery characteristic test for the multiple current rates and various temperature conditions.

2.5. Performance evaluation criteria and calculation

The mean squared error (MSE) is used to evaluate the effectiveness of the prediction results. The calculation procedure is shown in Equation (6).

$$MSE = \frac{1}{n} \sum_{i=1}^n (y_i - \hat{y}_i)^2 \quad (6)$$

In Equation (6), i is the value of data point at each time point, n is the total number of data points in the sample, and y_i is the actual SOC for each data point. The predicted value \hat{y}_i is compared with the actual SOC value at each time point t . The squared value is averaged and squared to obtain the minimized loss function of the linear regression. The root-mean-square error (RMSE) is the square root of the MSE between the predicted value and the actual value at each time point for the entire sequence n . The mathematical expression for the calculation of the RMSE is shown in Equation (7).

$$RMSE = \sqrt{\frac{1}{n} \sum_{i=1}^n (y_i - \hat{y}_i)^2} \quad (7)$$

In Equation (7), the RMSE is used to measure the deviation between the predicted value and the actual value, which is the error away from the mean. The mean absolute error (MAE) is introduced to evaluate the average absolute value of the error between the predicted value and the actual value. The mathematical expression for the MAE is shown in Equation (8).

$$MAE = \frac{1}{n} \sum_{i=1}^n |y_i - \hat{y}_i| \quad (8)$$

In Equation (8), the predicted value is completely consistent with the actual value. When the error is equal to 0, it means a perfect model. In this case, if the dispersion of the error is high, it means the maximum deviation is large, which increases the RMSE value. Also, the mean absolute percentage error (MAPE) is introduced, and its calculation is shown in Equation (9).

$$MAPE = \frac{100\%}{n} \sum_{i=1}^n \left| \frac{y_i - \hat{y}_i}{y_i} \right| \quad (9)$$

Equation (9) is the mathematical calculation expression for the MAPE, which ranges from 0–100%. A MAPE of 0% indicates a perfect model, whereas a MAPE of 100% indicates a poor model.

3. Experimental analysis

The test procedure is conducted for the whole-life-cycle process, including the evaluation of the temperature variations and the composite test process of OCV and HPPC. The working condition parameter initialization of the BBDST experiment. The aging characteristics verification is conducted, including the cyclic OCV change, capacity attenuation, pulse-current characteristic comparison, cut-off voltage change, and long-term charging energy attenuation to weaken the noise effect under complex working conditions.

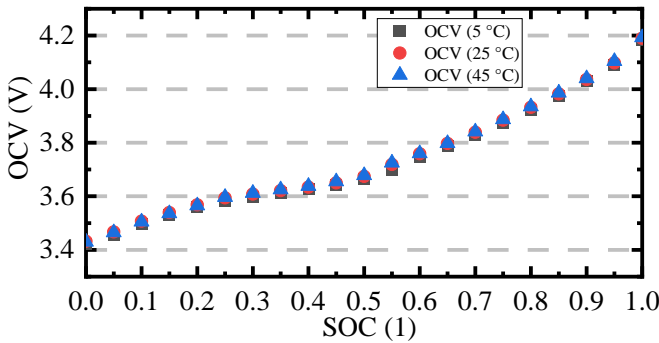
3.1. *Comparative cyclic OCV measurement and temperature variation under capacity fading effect*

The relevant data features are extracted from the original experimental data using effective processing methods. At different SOC levels, the relationship between internal parameters is obtained so that an accurate battery characteristic description is achieved. The dynamic working condition change includes the ambient temperature and current rate and is used to obtain the whole-life-cycle aging process characteristics. For the dynamic battery characteristics, a collaborative architecture is designed for each factor to express the impact on multi-time-scale state monitoring. Based on the detailed model, the changing law of OCV, capacity attenuation, temperature change, and inconsistent charge-discharge current rate characteristics are obtained. The composite HPPC test is performed at the same intervals as the SOC levels during the cyclic battery test.

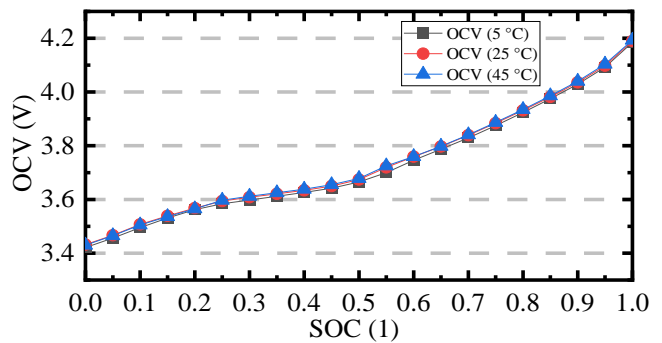
The interval between adjacent pulse power tests is one hour, in which the battery is discharged at a current rate of 1 C for 6 min at a SOC level reduction of 0.1. The voltage measurement is performed online, thereby defining the state relationship between all the internal parameters, including the OCV-SOC functional relationship, which has a nonlinear positive correlation until 3.356 V. The discrete points are obtained through an intermittent discharge process that achieves the overall variations through the curve fitting method. The functional relationship is obtained by mathematical analysis, which is then introduced into the battery modeling process under different temperature conditions. When the ambient temperature is high, the cut-off voltage is low, and the capacity is large

for the discharge. Then, the OCV changes correspond to the SOC variation, which shows a downward shift. At a low ambient temperature, the discharging cut-off voltage is high, so the battery power cannot be released efficiently.

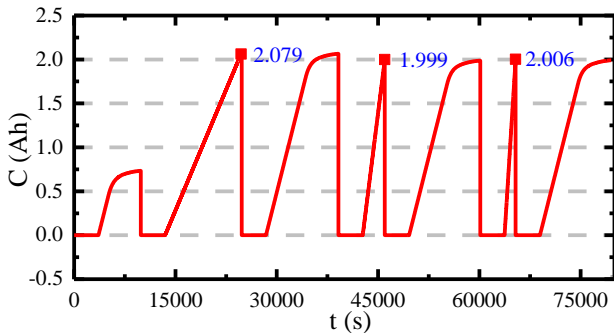
Experimental tests are conducted for the varying-temperature capacity fading characteristic test. When conducting the test, the battery working conditions are set to $T = 5, 25, \text{ and } 45 \text{ }^\circ\text{C}$ for the capacity test. The discharging capacity is measured and recorded for further comparison. The aging process is conducted for 200 cycles, and the capacity is measured after a long-term aging process, which is conducted at different working conditions at $T = 5, 25, \text{ and } 45 \text{ }^\circ\text{C}$ ambient temperatures and current rates of 0.3, 1.0, and 2.0 C. The final experimental results are compared with different working conditions. Subsequently, the varying-temperature capacity fading and voltage variation results are obtained, as shown in Figure 5.



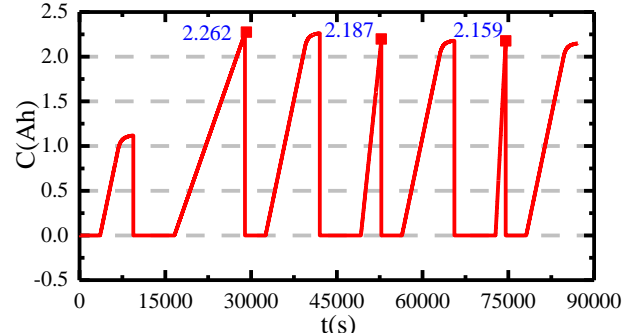
(a) Original OCV variation under varying temperature conditions



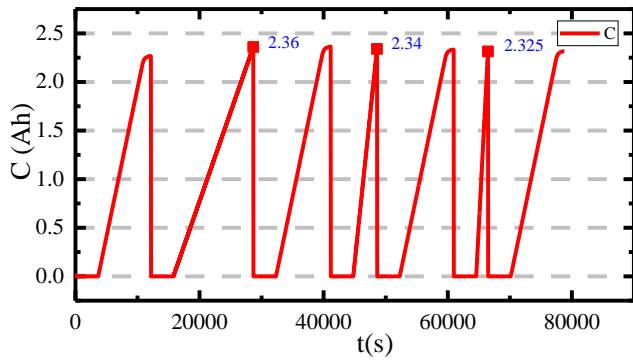
(b) Curve fitting results of the OCV variation under varying temperature conditions



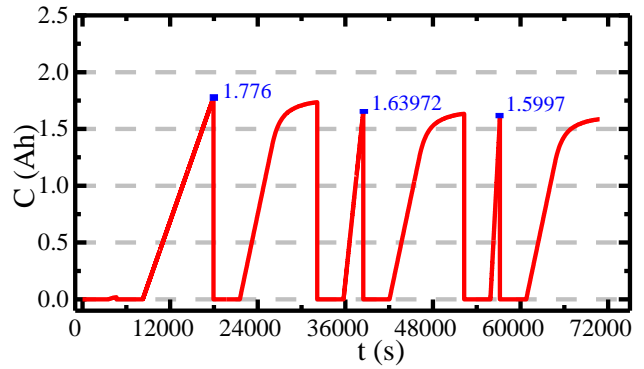
(c) Capacity variation for a new battery C7 when $T = 5 \text{ }^\circ\text{C}$



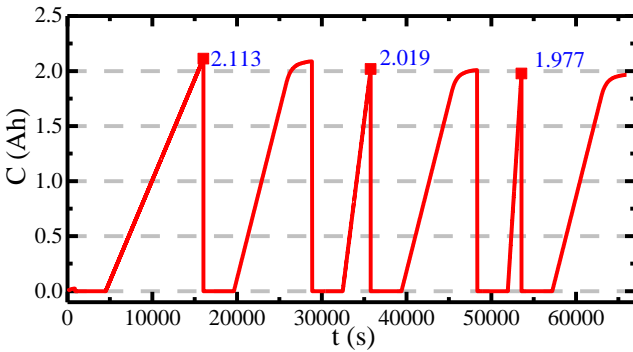
(d) Capacity variation for a new battery C7 when $T = 25 \text{ }^\circ\text{C}$



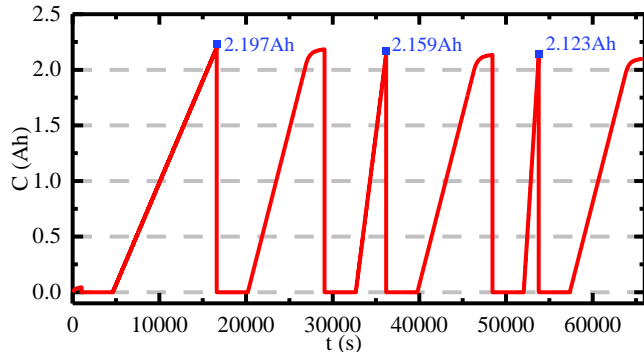
(e) Capacity variation for a new battery C7 when $T = 45\text{ }^{\circ}\text{C}$



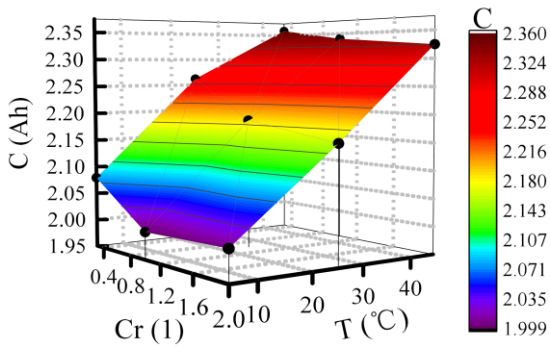
(f) Capacity variation for the aged battery C8 when $T = 5\text{ }^{\circ}\text{C}$



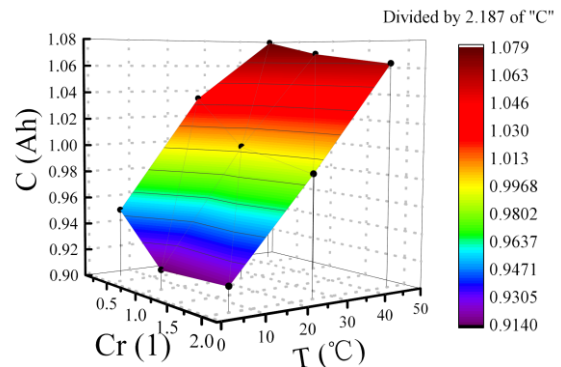
(g) Capacity variation for the aged battery C8 when $T = 25\text{ }^{\circ}\text{C}$



(h) Capacity variation for the aged battery C8 when $T = 45\text{ }^{\circ}\text{C}$



(i) Capacity variation for aging battery C7 under varying temperatures



(j) Normalized variation for aging battery C7 under varying temperatures

Figure 5. Experimental results for the cycling test under different temperature conditions

In Figure 5, the discharge capacity of the aging battery is significantly lower than that of the new battery at the same temperature. In this paper, Cr is the measured capacity value with the current rate that is obtained for the conditions of 0.3, 1.0, and 2.0 C for a temperature varying from 5 to 45 °C. The ambient temperature highly affects the battery discharge capacity in the experimental results. When the temperature is 5, 25, and 45 °C, the average discharge capacity of the new battery is 2.08, 2.203, and 2.30 Ah, respectively. The battery discharge capacity increases as the temperature rises. The discharge capacity trend of old batteries is similar, which provides an

effective reference to the working state management of whole-life-cycle lithium-ion batteries.

3.2. Pulse-current characteristics comparison

The voltage measurement is performed online to determine the battery cell status, thereby defining the inner factor relationship between each internal parameter, including the OCV-SOC variations. The 200 cyclic aging test is performed at a temperature of 25 °C. The experimental results are obtained from the first 20 test cycles where the battery voltage is observed to respond to the current changes. The experimental results of the aging test are obtained, as shown in Figure 6.

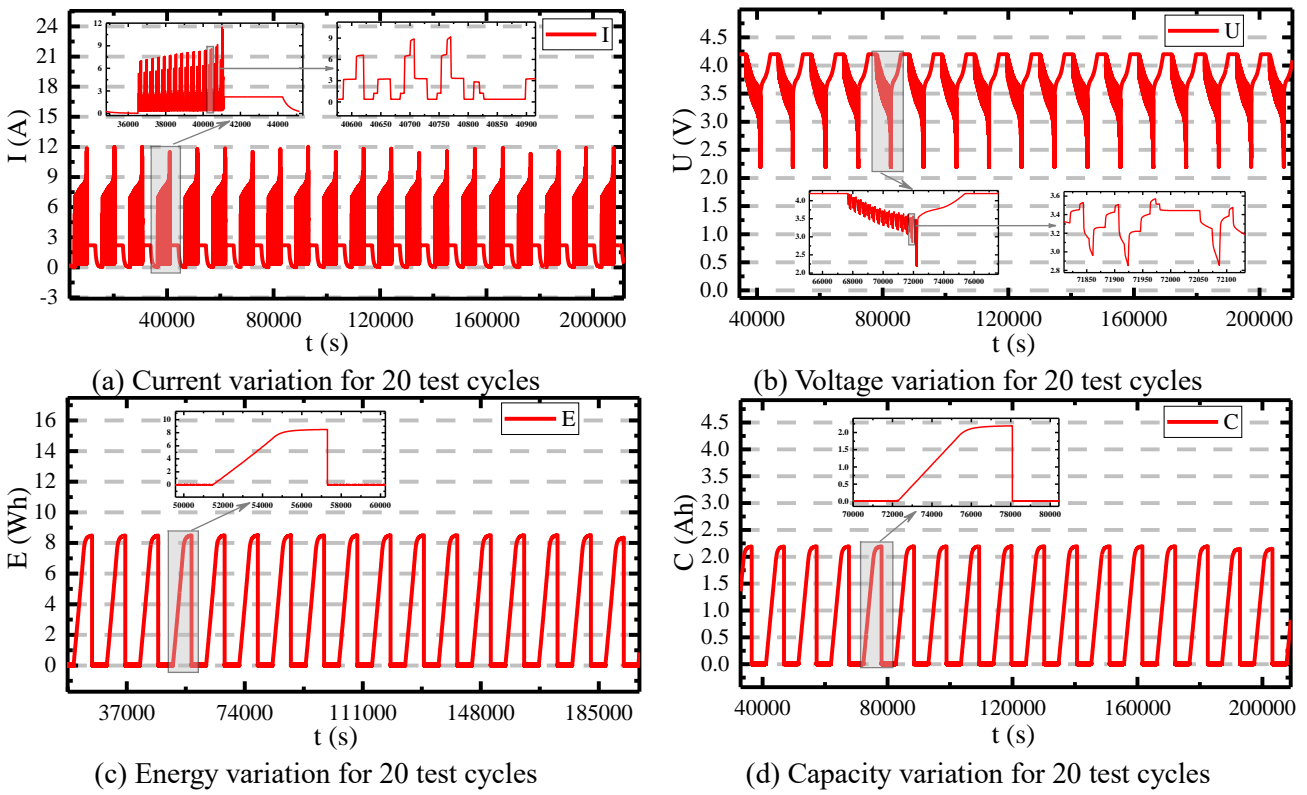


Figure 6. Experimental results for the cyclic aging test

In Figure 6, the battery voltage responds to current changes applied to the characteristic description of the whole-life-cycle batteries by combining the correction mechanism, thereby further improving the collaborative state prediction accuracy.

3.3. Long-term charging capacity attenuation

As for the long-term working conditions, the charging capacity is measured at the end of each last-time

charging process, which is used as a signal of the capacity variation after each 10-cycling BBDST working condition experiment. The surrounding temperature is set to be the same in each cyclic test that is fixed at 25°C. The external conditions vary highly from the inner part of the battery due to the current influence fluctuations and the ambient temperature. The charging capacity of the last cycle for the 10 cyclic tests for the battery C7 is obtained, as shown in Table 1.

Table 1. The charging capacity of the cyclic test for battery C7

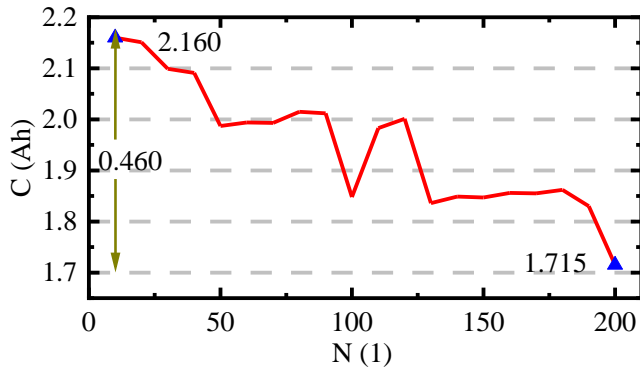
Test cycle	Charging capacity	Test cycle	Charging capacity
10	2.160	110	1.983
20	2.151	120	2.001
30	2.099	130	1.836
40	2.091	140	1.849
50	1.987	150	1.847
60	1.994	160	1.856
70	1.993	170	1.855
80	2.015	180	1.862
90	2.012	190	1.830
100	1.848	200	1.715

In Table 1, there are nonlinear changes in the charging capacity for the whole-life-cycle BBDST working condition experiment for battery C8. Another experimental test was carried out on battery C8 to analyze the effect of this nonlinear change. The experimental test results are obtained accordingly, as shown in Table 2.

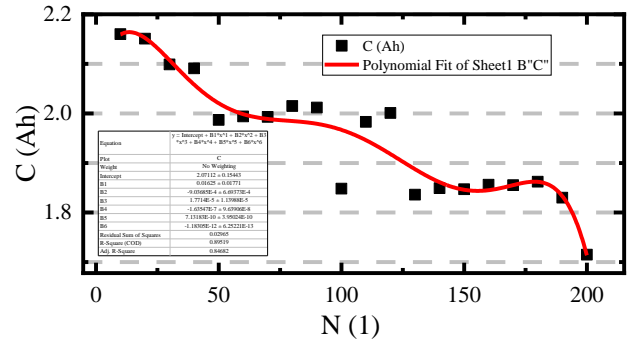
Table 2. The charging capacity of the cyclic test for battery C8

Test cycle	Charging capacity	Test cycle	Charging capacity
10	2.132	110	1.803
20	2.077	120	1.809
30	2.055	130	1.662
40	1.949	140	1.672
50	1.924	150	1.678
60	1.807	160	1.682
70	1.816	170	1.687
80	1.820	180	1.689
90	1.823	190	1.692
100	1.829	200	1.694

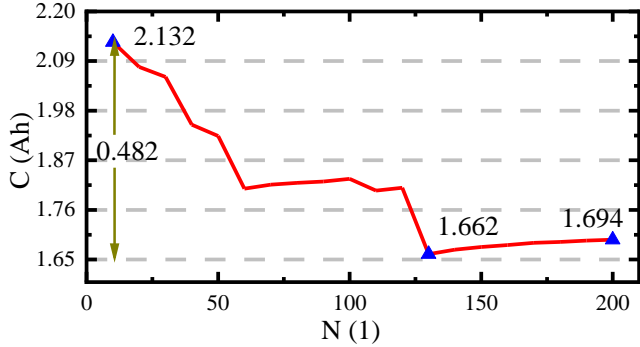
In Table 2, the table data is drawn as a graph for the detailed variations based on the experimental result. After the curve fitting method and special variation description, the charging capacity change of the experimental BBDST working condition is described accordingly, as shown in Figure 7.



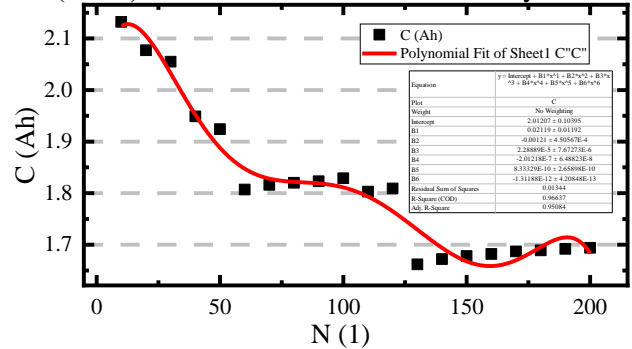
(a) Charging capacity variation for battery C7



(b) Charging capacity variation (dots) and deviation (curve) from the actual values for battery C7



(c) Charging capacity variation for battery C8



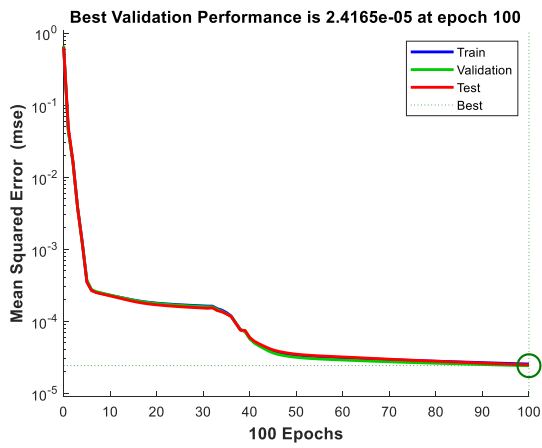
(d) Charging capacity variation (dots) and deviation (curve) from the actual values for battery C8

Figure 7. The charging capacity variation under the whole-life-cycle BBDST working condition

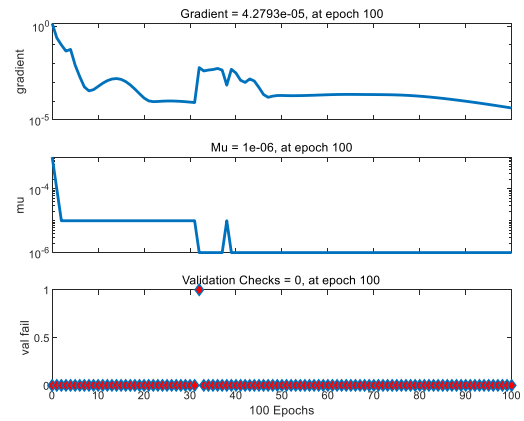
In Figure 7, the charging capacity changes as the cycle number increases, showing a monotonic decreasing order. By mathematically analyzing and comparing the results, the capacity changes for batteries C7 and C8 are 0.460 Ah and 0.482 Ah, respectively. The relative rate of capacity change of battery C7 is $0.460/2.160 * 100\% = 21.30\%$, and that of battery C8 is $0.482/2.132 * 100\% = 22.61\%$. For further power supply applications, it can provide an effective reference for the working state management of the whole-life-cycle of lithium-ion batteries.

3.4. SOC prediction for BBDST training and DST testing using the FF-LSTM method

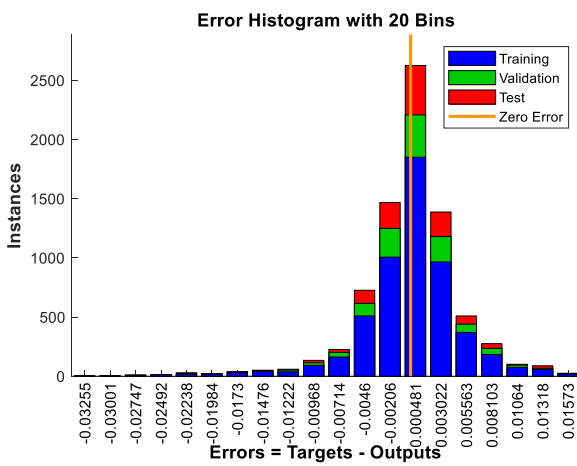
Various failure thresholds are used to realize the whole-life-cycle SOC prediction and verify the effectiveness of the proposed method. The FF-LSTM-based training and testing results of the whole-life-cycle SOC prediction are obtained and compared intuitively with the absolute errors, as shown in Figure 8.



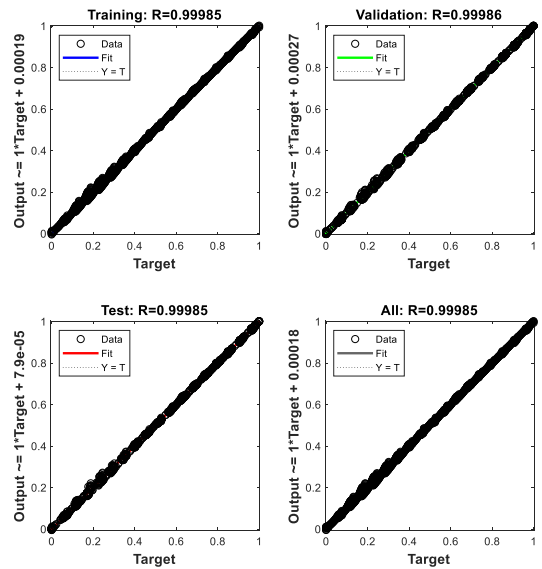
(a) FF-LSTM-based SOC prediction training validation curves



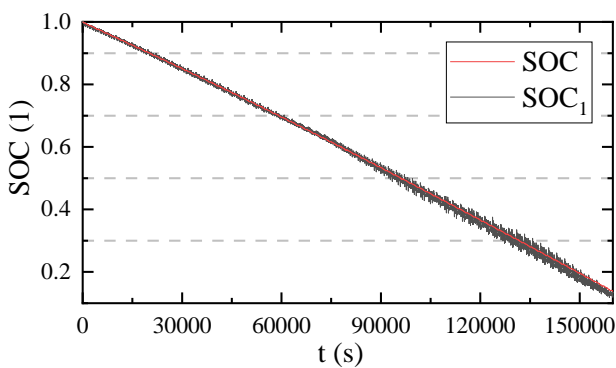
(b) FF-LSTM-based SOC prediction training performance curves



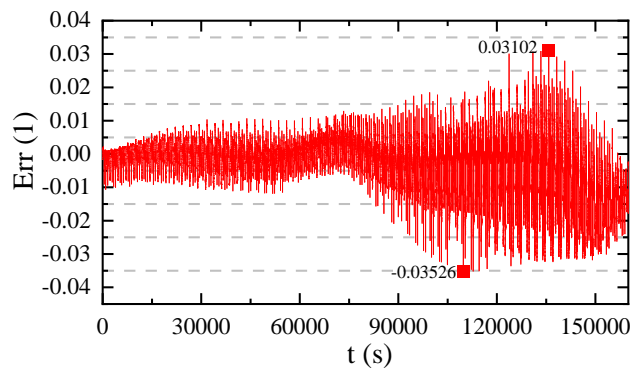
(c) FF-LSTM-based SOC prediction training error



(d) FF-LSTM-based SOC prediction training accuracy



(e) FF-LSTM-based SOC prediction curve



(f) Prediction error

Figure 8. The FF-LSTM-based training performance and SOC prediction under the complex DST working condition

Figure 8 shows the training performance of the FF-LSTM for SOC prediction. Figures 8 (e) and (f) are the SOC prediction results. In Figure 8 (e), SOC is the actual SOC, and SOC₁ is the predicted SOC₁ by the FF-LSTM method. It can

be observed in Figure 8 (f) that the maximum error is 3.53%, which demonstrates the effectiveness of the proposed FF-LSTM method with high accuracy and robustness over a long-term prediction period. The metric values of the prediction result obtained using the FF-LSTM method are low for the long-term prediction, with RMSE, MAE, and MAPE values of 3.451%, 2.541%, and 0.074%, respectively, under the complex DST working condition.

4. Conclusion

For the relevant parameter changing law of lithium-ion batteries along with the external temperature variations, an improved feedforward-long short-term memory (FF-LSTM) modeling method is proposed to realize the accurate whole-life-cycle SOC prediction by considering the current, voltage, and temperature variations. An optimized sliding balance window is constructed for the measured current filtering. Then, an improved steady-state screening model is constructed for the predicted SOC redundancy reduction. The core parameter change characteristics are obtained and analyzed under a long-term experimental dynamic stress test working condition. The long-term discharging capacity decay rate results show that the battery charging capacity reduces significantly with increasing time. The change in the charging capacity rate for batteries C7 and C8 is 21.30% and 22.61%, respectively, after 200 cycles. The maximum SOC prediction error is 3.53% with RMSE, MAE, and MAPE values of 3.451%, 2.541%, and 0.074%, respectively, under the complex DST working condition. The proposed FF-LSTM method lays the foundation for accurate state prediction in long-term operation conditions, improving energy management and safety.

Supplementary information

The whole-life-cycle testing results are available to all researchers using the link: <https://www.researchgate.net/project/Battery-life-test>.

Acknowledgment

The work was supported by the National Natural Science Foundation of China (Nos. 61801407 and 62173281), the Sichuan Science and Technology Program (No. 2019YFG0427), the China Scholarship Council (No. 201908515099), and the Fund of Robot Technology Used for Special Environment Key Laboratory of Sichuan Province (No. 18kftk03). Thanks to these sponsors

1. Gao, Y.Z., et al., *Health-Aware Multiobjective Optimal Charging Strategy With Coupled Electrochemical-Thermal-Aging Model for Lithium-Ion Battery*. IEEE Transactions on Industrial Informatics, 2020. **16**(5): p. 3417-3429.
2. Corno, M. and G. Pozzato, *Active Adaptive Battery Aging Management for Electric Vehicles*. Ieee Transactions on Vehicular Technology, 2020. **69**(1): p. 258-269.
3. Liu, K.L., et al., *Gaussian Process Regression With Automatic Relevance Determination Kernel for Calendar Aging Prediction of Lithium-Ion Batteries*. IEEE Transactions on Industrial Informatics, 2020. **16**(6): p. 3767-3777.
4. Tang, X.P., et al., *Model Migration Neural Network for Predicting Battery Aging Trajectories*. Ieee Transactions on Transportation Electrification, 2020. **6**(2): p. 363-374.
5. Zhu, J.G., et al., *Investigation of lithium-ion battery degradation mechanisms by combining differential voltage analysis and alternating current impedance*. Journal Of Power Sources, 2020. **448**(227575): p. 1-12.
6. Zhu, J.G., et al., *An improved electro-thermal battery model complemented by current dependent parameters for vehicular low temperature application*. Applied Energy, 2019. **248**(1): p. 149-161.
7. Zhao, X.C., et al., *Electrochemical-thermal modeling of lithium plating/stripping of Li (Ni_{0.6}Mn_{0.2}Co_{0.2})O₂/Carbon lithium-ion batteries at subzero ambient temperatures*. Journal of Power Sources, 2019. **418**(1): p. 61-73.
8. Shang, Y., et al., *A multi-fault diagnosis method based on modified Sample Entropy for lithium-ion battery strings*. Journal of Power Sources, 2020. **446**(227275): p. 1-12.
9. Wang, Q.K., et al., *State of Charge-Dependent Polynomial Equivalent Circuit Modeling for Electrochemical Impedance Spectroscopy of Lithium-Ion Batteries*. Ieee Transactions on Power Electronics, 2018. **33**(10): p. 8449-8460.
10. Han, L., X.H. Jiao, and Z. Zhang, *Recurrent Neural Network-Based Adaptive Energy Management Control Strategy of Plug-In Hybrid Electric Vehicles Considering Battery Aging*. Energies, 2020. **13**(1).
11. Pan, Y., et al., *Internal short circuit detection for lithium-ion battery pack with parallel-series hybrid connections*. Journal of Cleaner Production, 2020. **255**(120277): p. 1-10.
12. De Sutter, L., et al., *Battery aging assessment and parametric study of lithium-ion batteries by means of a fractional differential model*. Electrochimica Acta, 2019. **305**: p. 24-36.
13. Liu, K.L., et al., *Modified Gaussian Process Regression Models for Cyclic Capacity Prediction of Lithium-Ion Batteries*. Ieee Transactions on Transportation Electrification, 2019. **5**(4): p. 1225-1236.
14. Tagade, P., et al., *Deep Gaussian process regression for lithium-ion battery health prognosis and degradation mode diagnosis*. Journal of Power Sources, 2020. **445**: p. 1-14.
15. Dong, G.Z., et al., *Data-Driven Battery Health Prognosis Using Adaptive Brownian Motion Model*. Ieee Transactions on Industrial Informatics, 2020. **16**(7): p. 4736-4746.
16. Liu, K.L., et al., *An evaluation study of different modelling techniques for calendar ageing prediction of lithium-ion batteries*. Renewable & Sustainable Energy Reviews, 2020. **131**(110017): p. 1-14.
17. Li, K.Y., et al., *A Practical Lithium-Ion Battery Model for State of Energy and Voltage Responses Prediction Incorporating Temperature and Ageing Effects*. Ieee Transactions on Industrial Electronics, 2018. **65**(8): p. 6696-6708.

18. Tian, J.P., R. Xiong, and Q.Q. Yu, *Fractional-Order Model-Based Incremental Capacity Analysis for Degradation State Recognition of Lithium-Ion Batteries*. Ieee Transactions on Industrial Electronics, 2019. **66**(2): p. 1576-1584.
19. Tang, X.P., et al., *A novel framework for Lithium-ion battery modeling considering uncertainties of temperature and aging*. Energy Conversion and Management, 2019. **180**(1): p. 162-170.
20. Xiong, R., et al., *An electrochemical model based degradation state identification method of Lithium-ion battery for all-climate electric vehicles application*. Applied Energy, 2018. **219**(1): p. 264-275.
21. Ouyang, T.C., et al., *A novel state of charge estimation method for lithium-ion batteries based on bias compensation*. Energy, 2021. **226**(13): p. 1-13.
22. Li, X.Y., et al., *State-of-charge estimation tolerant of battery aging based on a physics-based model and an adaptive cubature Kalman filter*. Energy, 2021. **220**.
23. Jiang, C., et al., *A state-of-charge estimation method of the power lithium-ion battery in complex conditions based on adaptive square root extended Kalman filter*. Energy, 2021. **219**: p. 1-12.
24. Guo, Y.J., et al., *A compact and optimized neural network approach for battery state-of-charge estimation of energy storage system*. Energy, 2021. **219**.
25. Park, K.Y., et al., *Understanding capacity fading mechanism of thick electrodes for lithium-ion rechargeable batteries*. Journal of Power Sources, 2020. **468**(228369): p. 1-8.
26. Ghannoum, A. and P. Nieva, *Graphite lithiation and capacity fade monitoring of lithium ion batteries using optical fibers*. Journal of Energy Storage, 2020. **28**: p. 1-5.
27. Liu, X.Y.M. and C.B. Arnold, *Effects of Current Density on Defect-Induced Capacity Fade through Localized Plating in Lithium-Ion Batteries*. Journal of the Electrochemical Society, 2020. **167**(13): p. 1-13.
28. Gantenbein, S., et al., *Capacity Fade in Lithium-Ion Batteries and Cyclic Aging over Various State-of-Charge Ranges*. Sustainability, 2019. **11**(23): p. 1-15.
29. Pan, B., et al., *Aging mechanism diagnosis of lithium ion battery by open circuit voltage analysis*. Electrochimica Acta, 2020. **362**(137101): p. 1-8.
30. Rumberg, B., et al., *Identification of Li ion battery cell aging mechanisms by half-cell and full-cell open-circuit-voltage characteristic analysis*. Journal of Energy Storage, 2019. **25**: p. 1-11.
31. Laforgue, A., et al., *Effects of Fast Charging at Low Temperature on a High Energy Li-Ion Battery*. Journal of the Electrochemical Society, 2020. **167**(14): p. 1-12.
32. Rajmakers, L.H.J., et al., *A review on various temperature-indication methods for Li-ion batteries*. Applied Energy, 2019. **240**: p. 918-945.
33. Sun, D.M., et al., *State of charge estimation for lithium-ion battery based on an Intelligent Adaptive Extended Kalman Filter with improved noise estimator*. Energy, 2021. **214**: p. 1-14.
34. Zhang, Y.Z., et al., *Lithium-Ion Battery Remaining Useful Life Prediction With Box-Cox Transformation and Monte Carlo Simulation*. Ieee Transactions on Industrial Electronics, 2019. **66**(2): p. 1585-1597.
35. Zhu, R., et al., *Co-estimation of model parameters and state-of-charge for lithium-ion batteries with recursive restricted total least squares and unscented Kalman filter*. Applied Energy, 2020. **277**: p. 1-14.
36. Peng, N., et al., *Online parameters identification and state of charge estimation for lithium-ion batteries using improved adaptive dual unscented Kalman filter*. International Journal of Energy Research, 2020. **45**(7): p. 975-990.
37. Wen, A., et al., *Online Parameter Identification of the Lithium-Ion Battery with Refined Instrumental Variable Estimation*. Complexity, 2020. **2020**(8): p. 1-12.
38. Schneider, S.F., P. Novak, and T. Kober, *Rechargeable Batteries for Simultaneous Demand Peak Shaving and Price Arbitrage Business*. IEEE Transactions on Sustainable Energy, 2021. **12**(1): p. 148-157.
39. Zhengxin, J., et al., *An Immune Genetic Extended Kalman Particle Filter approach on state of charge estimation for lithium-ion battery*. Energy, 2021. **230**(52): p. 1-14.
40. Li, J.F., et al., *Aging modes analysis and physical parameter identification based on a simplified electrochemical model for lithium-ion batteries*. Journal of Energy Storage, 2020. **31**(6): p. 1-13.

41. Ren, B.Y., et al., *Parameter identification of a lithium-ion battery based on the improved recursive least square algorithm*. Iet Power Electronics, 2020. **13**(12): p. 2531-2537.
42. Saleem, K., K. Mehran, and Z. Ali, *Online reduced complexity parameter estimation technique for equivalent circuit model of lithium-ion battery*. Electric Power Systems Research, 2020. **185**: p. 1-12.
43. Garg, A., et al., *Aging model development based on multidisciplinary parameters for lithium-ion batteries*. International Journal of Energy Research, 2020. **44**(4): p. 2801-2818.
44. Tan, C.M., P. Singh, and C. Chen, *Accurate Real Time On-Line Estimation of State-of-Health and Remaining Useful Life of Li ion Batteries*. Applied Sciences-Basel, 2020. **10**(21): p. 1-16.
45. Sandoval-Chileno, M.A., et al., *Robust State of Charge estimation for Li-ion batteries based on Extended State Observers*. Journal of Energy Storage, 2020. **31**: p. 1-13.
46. Antonucci, V., et al., *Li-ion Battery Modeling and State of Charge Estimation Method Including the Hysteresis Effect*. Electronics, 2019. **8**(11): p. 1-19.
47. Feng, X.N., et al., *Online State-of-Health Estimation for Li-Ion Battery Using Partial Charging Segment Based on Support Vector Machine*. Ieee Transactions on Vehicular Technology, 2019. **68**(9): p. 8583-8592.
48. Avila, L.O., et al., *State of charge monitoring of Li-ion batteries for electric vehicles using GP filtering*. Journal of Energy Storage, 2019. **25**: p. 1-9.
49. Liu, H.L., et al., *The performance management of a Li-ion battery by using tree-like mini-channel heat sinks: Experimental and numerical optimization*. Energy, 2019. **189**: p. 1-15.
50. Lee, J., D. Kwon, and M.G. Pecht, *Reduction of Li-ion Battery Qualification Time Based on Prognostics and Health Management*. Ieee Transactions on Industrial Electronics, 2019. **66**(9): p. 7310-7315.
51. Rao, Z.H. and X. Zhang, *Investigation on thermal management performance of wedge-shaped microchannels for rectangular Li-ion batteries*. International Journal of Energy Research, 2019. **43**(8): p. 3876-3890.
52. Wang, Y., M. Li, and Z. Chen, *Experimental study of fractional-order models for lithium-ion battery and ultra-capacitor: Modeling, system identification, and validation*. Applied Energy, 2020. **278**(115736): p. 1-11.
53. Du, J., et al., *Impact of high-power charging on the durability and safety of lithium batteries used in long-range battery electric vehicles*. Applied Energy, 2019. **255**(113793): p. 1-10.
54. Hu, X.S., et al., *Battery Lifetime Prognostics*. Joule, 2020. **4**(2): p. 310-346.
55. Wang, S.L., et al., *A novel power state evaluation method for the lithium battery packs based on the improved external measurable parameter coupling model*. Journal of Cleaner Production, 2020. **242**(118506): p. 1-13.
56. Wang, S.L., et al., *Open circuit voltage and state of charge relationship functional optimization for the working state monitoring of the aerial lithium-ion battery pack*. Journal of Cleaner Production, 2018. **198**(1): p. 1090-1104.
57. Wang, S.L., et al., *A novel charged state prediction method of the lithium ion battery packs based on the composite equivalent modeling and improved spline Kalman filtering algorithm*. Journal of Power Sources, 2020. **471**(228450): p. 1-13.
58. Wang, S.L., et al., *A novel safety anticipation estimation method for the aerial lithium-ion battery pack based on the real-time detection and filtering*. Journal of Cleaner Production, 2018. **185**(1): p. 187-197.
59. Sarkar, A., et al., *Chemo-economic analysis of battery aging and capacity fade in lithium-ion battery*. Journal of Energy Storage, 2019. **25**(100911): p. 1-8.
60. Marques, P., et al., *Comparative life cycle assessment of lithium-ion batteries for electric vehicles addressing capacity fade*. Journal of Cleaner Production, 2019. **229**: p. 787-794.
61. Kuo, T.J., *Development of a Comprehensive Model for the Coulombic Efficiency and Capacity Fade of LiFePO₄ Batteries under Different Aging Conditions*. Applied Sciences-Basel, 2019. **9**(21): p. 1-20.